

Metasurface-Based Realization of Photonic Time Crystals

X. Wang^{1,3,*}, M. S. Mirmoosa¹, V. S. Asadchy^{1,2}, C. Rockstuhl^{3,4}, S. Fan², and S. A. Tretyakov¹

¹*Department of Electronics and Nanoengineering,*

Aalto University, P.O. Box 15500, FI-00076 Aalto, Finland

²*Ginzton Laboratory and Department of Electrical Engineering,
Stanford University, Stanford, California 94305, USA*

³*Institute of Theoretical Solid State Physics, Karlsruhe Institute of Technology, 76131 Karlsruhe, Germany*

⁴*Institute of Nanotechnology, Karlsruhe Institute of Technology, 76131 Karlsruhe, Germany*

Photonic time crystals are artificial materials whose electromagnetic properties are uniform in space but periodically vary in time. The synthesis of such materials and experimental observation of their physics remain very challenging. In this work, we extend the concept of photonic time crystals to metasurfaces. We demonstrate that time-varying metasurfaces preserve key physical properties of volumetric time crystals, in particular, generating momentum bandgaps for surface and free-space waves. Moreover, in sharp contrast to bulk time-crystals, the momentum bandgap can be directly accessed by free-space excitations, significantly simplifying the crystal implementation and its exploitation. Based on a microwave metasurface design, we achieved the first experimental confirmation of exponential wave amplification inside a momentum bandgap. The proposed metasurface serves as a universal material platform for realizing exotic photonic space-time crystals and providing low-noise amplification for surface wave signals in future 6G wireless communications.

INTRODUCTION

Time, as an additional degree of freedom, has significantly extended the potential of artificial electromagnetic materials [1–3]. In the past few years, numerous new physical effects have been discovered based on time modulation of material properties, such as magnetless nonreciprocity [4, 5], effective magnetic field for photons [6, 7], synthetic dimensions [8–11], electromagnetic devices beyond physical bounds [12, 13], among many others [1]. One of the major developments in this direction is the concept of photonic time crystals (PhTCs) [14, 15]. PhTCs are artificial materials whose electromagnetic properties (such as permittivity or permeability) are periodically and rapidly modulated in time while remaining uniform in space. They are temporal counterparts of spatial photonic crystals [16]. In analogy to frequency bandgaps in spatial photonic crystals, the temporal modulation of PhTCs results in momentum bandgaps. Due to the non-Hermitian nature of PhTCs, inside the momentum bandgap, the electromagnetic wave grows exponentially in time [8]. This is in sharp contrast to wave attenuation in time occurring inside a frequency bandgap [16, 17]. Recently, numerous interesting wave phenomena have been theoretically predicted in PhTCs, such as topologically nontrivial phases [8], a temporal analog of Anderson localization [18, 19], amplified radiation from free electrons and atoms [15, 20], etc.

Until now, most studies on PhTCs contained theoretical predictions, and the experimental verification of the new and intriguing wave effects was rarely reported. Moreover, the reported experiments were limited to voltage waves in transmission lines [21] and water waves [22]. Implementing genuine photonic time crystals for electromagnetic waves implies temporal modulation of a bulk

material, which is a significant challenge. While there have been several important developments toward the implementation of PhTCs in the optical regime based on epsilon-near-zero materials [23–25], considerable challenges remain due to the following reasons. First, PhTCs require a fast temporal variation of the material properties at about twice the operational frequency of the probing electromagnetic field. Such rapid oscillation is difficult to achieve given the finite excitation and recombination times in the aforementioned materials (currently in the range of a few THz [23]). Moreover, the temporal modulation with a uniform phase of a bulk three-dimensional material is nontrivial and needs precise engineering of the optical pump.

In this work, we extend the concept of PhTCs to metasurfaces, which are two-dimensional electromagnetic structures. By varying in time their surface property, our metasurface structure provides a universal and robust platform to explore the physics of PhTCs. We show that temporal metasurfaces give rise to momentum bandgaps for surface and free-space propagating waves. Moreover, the metasurface platform provides a qualitatively new route for accessing photonic momentum bandgaps by enabling direct excitation of the structure from free-space. We experimentally observe electromagnetic wave amplification in the momentum bandgap. This amplification is the key feature of PhTCs that has not been observed in earlier experiments [21]. Finally, we highlight a qualitative difference between PhTCs and degenerate parametric amplifiers.

EIGENMODE ANALYSIS

Figure 1A shows a spatially homogeneous metasurface at the $z = 0$ plane. The metasurface is modeled as a ca-

capacitive impenetrable surface impedance boundary [17]. The effective capacitance of the boundary is periodically modulated in time as $C(t) = C(t + T_m)$, where T_m is the modulation period. An arbitrary periodic modulation function can be expressed as a sum of Fourier terms, $C(t) = \sum_p c_p e^{jp\omega_m t}$, where $p \in \mathbb{Z}$ is the Fourier index, c_p are the Fourier coefficients, and $\omega_m = 2\pi/T_m$ is the modulation frequency. Here, we assume that fields vary in time according to $e^{j\omega t}$ convention. We consider TE-polarized eigenwaves of this time-varying boundary that propagate along the x -direction. The temporal modulation induces an infinite number of frequency harmonics $\omega_n = \omega_0 + n\omega_m$, where ω_0 is the frequency of the fundamental harmonic and n is the Floquet order. For each value of wavenumber β , the tangential electric (along y -direction) and magnetic fields (along x -direction) of the eigenmode are expressed as a sum of these harmonics:

$$\vec{E} = \sum_n E_n e^{-\alpha_n z} e^{-j(\beta x - \omega_n t)} \hat{y}, \quad (1a)$$

$$\vec{H} = \sum_n H_n e^{-\alpha_n z} e^{-j(\beta x - \omega_n t)} \hat{x}, \quad (1b)$$

where α_n denotes the attenuation constants along the z -direction regarding each harmonic, E_n and H_n are spectral amplitudes related by wave admittance, i.e., $H_n = (\alpha_n / j\omega_n \mu_0) E_n$. Since every harmonic must satisfy the Helmholtz equation in free-space, we obtain the condition $\beta^2 = \alpha_n^2 + \omega_n^2 \epsilon_0 \mu_0$. Additionally, by substituting (1b) into the time-domain boundary condition $\int \hat{z} \times \vec{H} dt = C(t) \vec{E}$ of a capacitive surface, we also obtain (see supplementary section S1 [26])

$$\sum_p j\omega_n c_p E_{n-p} = H_n. \quad (2)$$

The spectral content of the harmonics is truncated with Floquet orders from $n = -N$ to $n = +N$. Because all the considered harmonics must satisfy Eq. (2), we have in total $2N + 1$ equations that are written in a matrix form $\mathbf{Y} \cdot \mathbf{E} = \mathbf{H}$. Here, \mathbf{Y} is a square matrix related to the Fourier coefficients c_p and frequencies ω_n , \mathbf{E} and \mathbf{H} are column vectors containing harmonics E_n and H_n , respectively. By combining this matrix equation with $\mathbf{M} \cdot \mathbf{E} = \mathbf{H}$ that relates the electric and magnetic field column-vectors through the admittance matrix \mathbf{M} , we finally deduce the following equation:

$$[\mathbf{Y} - \mathbf{M}] \cdot \mathbf{E} = 0. \quad (3)$$

The definitions of the matrices are shown in supplementary section S2 [26]. Thus, according to the above expression, the dispersion relation for waves propagating along time-varying capacitive boundaries is given by $\det[\mathbf{Y} - \mathbf{M}] = 0$, in which \det denotes the determinant.

As a specific example, we consider a boundary whose effective surface capacitance is modulated according to

$C(t) = C_0[1 + 0.3 \cos(\omega_m t)]$. The median surface capacitance is expressed through the surface admittance as $C_0 = Y_s / j\omega_0$, where $Y_s = 2.5 \times 10^{-3}$ S is assumed. The band diagram for this case is depicted with a blue line in Fig. 1(B). Analogously to the space-modulated boundaries where frequency bandgaps occur [16, 17], for the time-modulated boundary, the corresponding bandgap is generated in the k -space, as the figure confirms. Inside the momentum bandgap, frequencies ω are complex-valued.

WAVE PROPAGATION INSIDE A MOMENTUM BANDGAP

It is also possible to determine eigenmodes inside the bandgap by solving equation (3) with respect to the frequency. As an example, we choose the wavenumber in the center of the momentum bandgap $\beta_g = 0.69\beta_m$. The corresponding eigenfrequencies (see the colored points in Fig. 1(B)) are complex values given by $\omega_n = (0.5 + n \pm j0.023)\omega_m$, where $+j$ and $-j$ indicate that the harmonic exponentially decays or grows in time, respectively. All these frequency harmonics exist simultaneously with specific amplitudes and phases that satisfy equation (3). The spectral content E_n of the growing and decaying eigenmodes for β_g is shown in Fig. 1C. Since the decaying harmonics eventually disappear as time passes, we only consider amplified harmonics hereafter.

It is observed that the harmonic amplitudes are symmetrically distributed in the spectrum. The $n = 0$ and $n = -1$ harmonics are dominant and propagate along the capacitive boundary with equal amplitudes, but the real parts of their frequencies have opposite signs. These two harmonics have opposite phase velocities $v_{ph} = \text{Re}(\omega)/\beta$ and together form a standing surface wave with a temporally growing amplitude. Importantly, the higher-order harmonics ($n > 0$ and $n < -1$) for the considered scenario are outside the light cone and correspond to free-space propagating waves. This means that the temporal modulation not only excites surface harmonics but additionally results in coupling of surface harmonics to free-space propagating harmonics, and all these harmonics have the same amplification rate.

Next, we numerically verify the wave evolution in the momentum bandgap. First, we consider the scenario where the momentum bandgap is probed by surface-wave excitations. From the time $t = 0$ until $t = 30T_m$ ($T_m = 2\pi/\omega_m$), a surface wave is launched onto the stationary (or static) capacitive boundary $C(t) = C_0$ with $\omega = 0.5\omega_m$ and $\beta = 0.69\beta_m$ from the left simulation port located above the boundary (see Fig. 1D). After $t > 30T_m$, the temporal modulation of the capacitive boundary is turned on. Since the modulation occurs in time and the structure remains uniform in space, the momentum of the waves remains unchanged. However, the

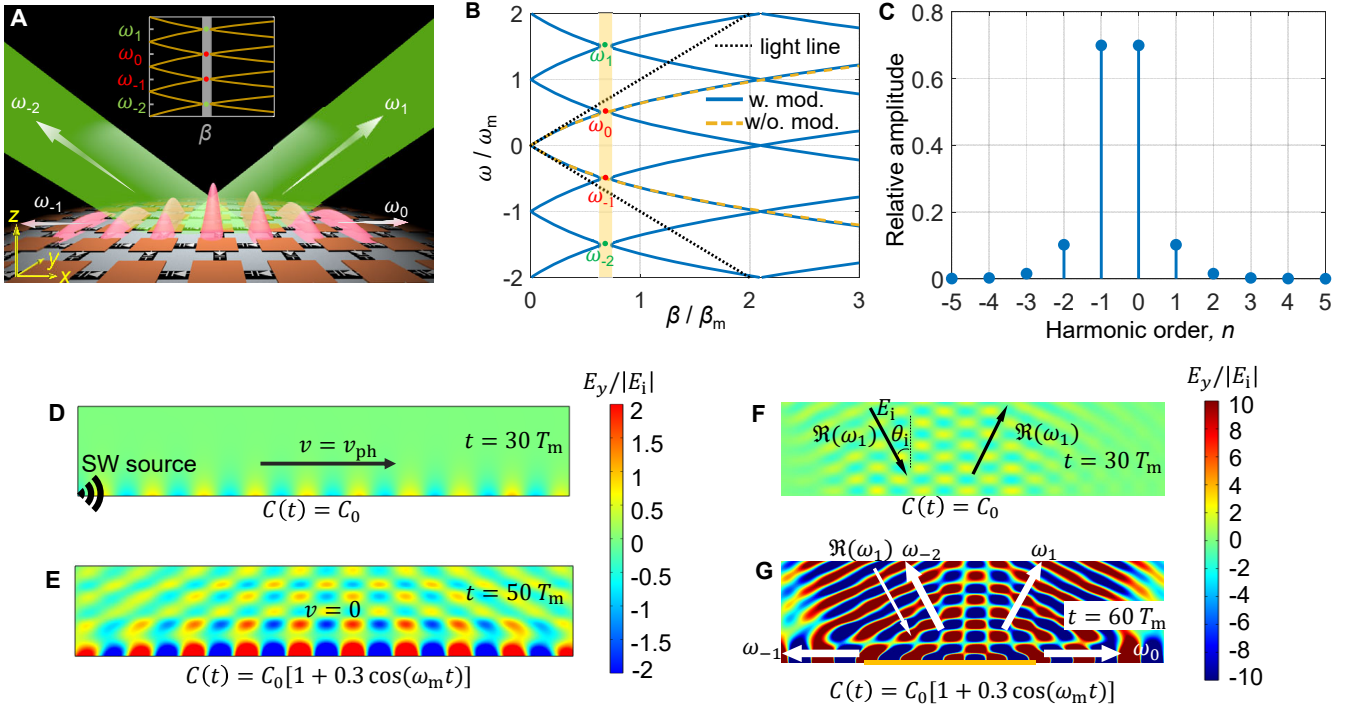


FIG. 1. (A) Conceptual picture of the metasurface PhTCs. The momentum bandgap (grey gap in the inset) opens when the surface properties are uniformly modulated in time. In the bandgap, multiple harmonics are symmetrically excited with different frequencies but the same wavevector. (B) Band structure (blue solid line) and bandgap (orange area) of the time-varying capacitive boundary. The dispersion curve of the time-invariant boundary (red dashed line) is derived in the supplementary section S3 [26]. The horizontal axis depicts the wavevector normalized to $\beta_m = \omega_m \sqrt{\epsilon_0 \mu_0}$. The band diagram is periodic along the frequency axis. (C) Spectral composition of electric-field harmonics in the eigenmodes inside the momentum bandgap with $\beta_g = 0.69\beta_m$. (D) Electric field distributions above the boundary at $t = 30T_m$ and (E) $t = 50T_m$. The fields are normalized to the surface wave excitation amplitude $|E_i|$. (F) Electric field distribution above the boundary under plane wave incidence at $t = 30T_m$ and (G) $t = 60T_m$. All the field simulations in this figure are obtained from COMSOL Multiphysics.

modulation generates backward and forward surface harmonics with equal amplitudes (see Fig. 1C), resulting in a standing wave along the horizontal direction with zero group velocity, as shown in Fig. 1E. Together with the surface harmonics, free-space harmonics are symmetrically generated and exponentially amplified in time (according to Fig. 1C). The complete field evolution animation is available as a Supplementary Video.

Furthermore, since, according to Fig. 1B, the momentum gap splits bands corresponding to both surface waves and free-space waves, it is feasible to access the momentum gap by obliquely illuminating the boundary with an *external* plane wave at the tangential wavevector β_g and frequency $\Re(\omega_1)$. In a second set of simulations, from the time $t = 0$ until $t = 30T_m$, we launch onto the time-invariant boundary such free-space plane wave at the incident angle $\theta_i = \arcsin[c\beta_g/\Re(\omega_1)]$ (see Fig. 1F). The reactive boundary fully reflects the incident wave, forming a standing wave pattern in the normal direction. The temporal modulations of the boundary are turned on after $t = 30T_m$ in a finite region (marked by orange color in Fig. 1G). The temporal modulation excites surface harmonics (β_g, ω_0) and (β_g, ω_{-1}) , as well as plane-

wave harmonics which include (β_g, ω_1) and (β_g, ω_{-2}) . All these harmonics experience exponential growth at the same rates. Therefore, the boundary effectively acts as a bulk PhTC that amplifies free-space harmonics inside the momentum bandgap. Such configuration is unique to metasurface-based PhTCs and provides a useful route for studying the physics of photonic momentum bandgaps.

METASURFACE DESIGN AT MICROWAVE FREQUENCIES

As a proof of concept, we design a metasurface for operation at microwave frequencies and experimentally explore the momentum bandgap for surface waves. Figure 2A shows the unit cell of the suggested metasurface. The capacitive impenetrable metasurface is implemented by a periodic arrangement of metallic strips in the xy -plane over a grounded substrate [17]. On the top side, two metal strips are separated by a gap that provides capacitive coupling for TE-polarized surface waves. To modulate the effective capacitance of the unit cell in time, the metallic strips are connected through via

and a varactor diode located below the bottom metalization layer. The cathode of the diode is biased with a static voltage $V_{dc} = 3.5$ V to provide the average capacitance value of the varactor $C_{av} = 4$ pF (different from the effective capacitance of the unit cell). Using full-wave simulations in CST Studio Suite, the effective surface capacitance of the time-invariant unit cell is estimated as $C_0 = 0.95$ pF. At frequencies below 1 GHz, the time-invariant unit cell supports only one eigenmode in TE polarization (see the band structure in Fig. S1 in [26]). The surface wave is most efficiently transmitted at around $f_s = 870$ MHz, with the wavelength of $\lambda_s \approx 4D_x$, as shown in Fig. S2 [26].

The metasurface of finite size comprises eight described unit cells along the x -direction. Since the metasurface operates in TE polarization (electric field along the y -direction), the periodic arrangement of the unit cells along the y -direction is conveniently emulated by placing vertical conducting walls (parallel to the xz -plane) at $y = \pm D_y/2$ (see the geometry of the metasurface in Fig. S3 [26]). The sinusoidal modulation signal $V_{mod}(t) = V_0 \sin(2\pi f_m t)$ with $f_m = 2f_s$ was injected into a 1×4 power divider to modulate the capacitance of the four unit cells. Numerical simulations show that modulating only four out of eight unit cells (approximately one-wavelength area) is sufficient to achieve amplification (see Fig. S5 in [26]). The amplification factor is largely insensitive to the phase of the incident wave (see related discussions on phase sensitivity in the supplementary section S6 [26]).

EXPERIMENTAL DEMONSTRATION

The fabricated metasurface-based PhTC is shown in Fig. 2B. Before switching on the modulation, the operating frequency of the metasurface is determined as $f_s = 871$ MHz by measuring the maximum transmission for surface waves traveling through the metasurface (see Fig. S2 in [26]).

Next, we investigate the surface wave transmission when temporal modulations are turned on. The experimental setup can be seen in Fig. 2B. The metasurface has three ports: left (input), right (output), and the middle port, wherein the modulation signal $V_{mod}(t)$ is applied. The input port is connected to signal generator 1 that generates a signal surface wave at $f_s = 871$ MHz. The input power is set at $P_{in} = -10$ dBm. The output port is connected to a spectrum analyzer. The modulation is generated by an independent generator 2 with a frequency twice the signal frequency $f_m = 2f_s = 1742$ MHz to ensure that the incident surface wave falls into the stopband. The modulation signal enters into a 4-way microstrip power divider which is connected to the four unit cells of the metasurface.

Figure 2C shows the spectrum of the signal received at

Port 2 inside the momentum bandgap. In the absence of modulation, there is only the signal frequency harmonic with power $P_{out}(f_s) = -39.14$ dBm. When the modulation signal is exerted at the middle port with +27 dBm power, the output power of the fundamental frequency components increases to $P_{out}(f_s) = -14.13$ dBm, that is, with 25 dB gain. The amplification of the surface wave occurs because the incident signal wave has a wavenumber inside the momentum bandgap induced by the temporal modulation. When no signal wave is present and the modulation is on, the output port detects only frequency harmonic f_m (see yellow dashed line in Fig. 2C), which means that the metasurface does not reach the unstable regime of parametric self-oscillations. While working in the parametric-amplification regime, the PhTC exhibits a finite gain: Radiation losses due to a finite-size geometry compensate for the exponential signal growth. The power of the surface wave at f_s received at Port 2 increases exponentially with the strength of the temporal modulations $P_m = V_0^2/2R_s$ (here $R_s = 50$ Ohm is the source resistance), as shown in Fig. 2D. Further increase of the modulation strength would lead to parametric self-oscillation whose amplitude would be limited due to the departing from the linear regime of the varactor diode [27, Sec. 10.8].

It is also important to experimentally confirm the non-amplification effect for excitations outside the momentum bandgap. To depart from the bandgap, it is sufficient to shift the modulation frequency away from the value $f_m = 2f_s$ (keeping constant f_s). In this way, the band structure of the PhTC will be modified (the band structure is uniquely determined by the metasurface structure and the modulation frequency), and the signal surface harmonic with parameters (β_s, f_s) will no longer belong to the momentum bandgap. The inset in Fig. 2E depicts numerically calculated bandgaps for two scenarios with different modulation frequencies. The black point denotes the signal surface harmonic. As is seen, for the modulation frequency $f_m = 1637$ MHz, the incident wave resides outside the bandgap. The primary plot in Fig. 2E indicates the measured amplification gain of the PhTC at the signal frequency $f_s = 871$ MHz versus modulation frequency $f_m \leq 2f_s$. When the modulation frequency is close to twice the incident frequency, amplification is maximum because the wave is in the center of the bandgap (see the blue curve in the inset). As the modulation frequency reduces, the amplification rate decreases, crossing zero below 1637 MHz.

It is worth mentioning that the amplification effect of incident surface wave obtained in both simulations and experiments is nearly phase-insensitive. Therefore, the PhTC does not require phase synchronization between incident and modulation signals. Such a property fundamentally differs from conventional degenerate parametric amplifiers operating in the stable regime (see supplementary section S7 in [26] for more details).

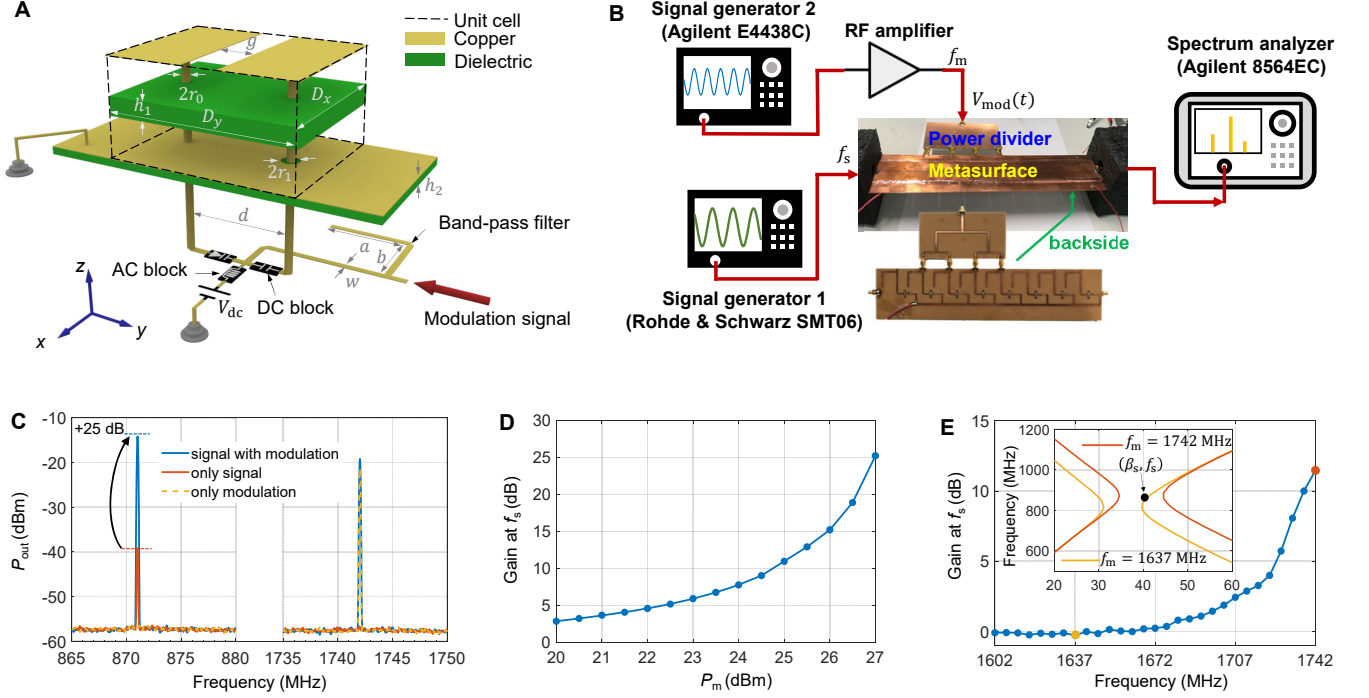


FIG. 2. (A) Unit cell of the metasurface-based PhTC (denoted in a dashed frame). The unit cell is periodically repeated in the xy -plane. Here, for clearer illustration, the three layers with metallic patterns (upper layer with strips, middle ground plane, and lower layer with circuitry) are visually separated from the dielectric substrates. To prevent the crosstalk of the surface wave with the modulation source, an L-shaped microstrip band-pass filter is connected to the bias circuit. The structural parameters are $g = 1.0$ mm, $r_1 = 2r_0 = 2.0$ mm, $D_x = 40$ mm, $D_y = 50$ mm, $h_1 = 2.4$ mm, $h_2 = 1.0$ mm, $d = 9.0$ mm, $a = 25.6$ mm, $b = 21.0$ mm, and $w = 2.0$ mm. The dielectric substrate is FR4 with permittivity $\epsilon_r = 4.2(1 - j0.025)$. (B) Experiment setup. The black modules at two terminals are microwave absorbers. Since the output voltage of the signal generator 2 is limited, a radio-frequency voltage amplifier with 40 dBm gain is connected to improve the modulation amplitude. (C) Frequency spectrum of the received power at the output port for three different scenarios. (D) Dependence of the amplification gain at $f_s = 871$ MHz on the power of the modulation signal. (E) Amplification gain of the surface wave at $f_s = 871$ MHz versus the modulation frequency f_m . The modulation strength is kept constant at 25 dBm. The green point represents the incident surface harmonics (β_s, f_s) . The band structure is obtained numerically, for the extracted value of effective capacitance of the modulated metasurface is $C(t) = C_0[1 - 0.31 \cos(2\pi f_m t)]$, where $C_0 = 0.95$ pF.

CONCLUSION

This work demonstrates that a temporally modulated metasurface offers equivalent wave effects to bulk three-dimensional PhTCs. We have experimentally verified the existence of momentum bandgap in such two-dimensional PhTCs and strong wave amplification inside it. Furthermore, it is shown that a metasurface-based PhTC can be excited externally by plane waves, amplifying both surface-bounded and free-space harmonics. The proposed metasurface platform can significantly simplify the construction and exploration of PhTCs, providing great convenience for probing the physics in PhTCs and photonic space-time crystals [28, 29]. From the application point of view, the demonstrated metasurface PhTCs can become an important contribution to surface wave communications, serving as a “filling station” for surface-wave signals. In particular, recently suggested surface-wave-assisted reconfigurable intelligent

surfaces [30] would enormously benefit from the amplification functionality of introduced metasurfaces. Such surfaces are predicted to operate as smart radio environments, playing a central role in future 6G wireless communications. Furthermore, it is possible to extend the proposed concept to higher frequencies, e.g., the terahertz range, with graphene under optical pumping, and even to optical frequencies using nonlinear thin films, realizing non-resonant, tunable, and ultra-thin optical lasers.

* xuchen.wang@aalto.fi

- [1] E. Galiffi, *et al.*, *Advanced Photonics* **4**, 014002 (2022).
- [2] A. M. Shaltout, V. M. Shalaev, M. L. Brongersma, *Science* **364**, eaat3100 (2019).
- [3] N. Engheta, *Nanophotonics* **10**, 639 (2021).
- [4] Z. Yu, S. Fan, *Nature Photonics* **3**, 91 (2009).

- [5] N. A. Estep, D. L. Sounas, J. Soric, A. Alù, *Nature Physics* **10**, 923 (2014).
- [6] K. Fang, Z. Yu, S. Fan, *Nature Photonics* **6**, 782 (2012).
- [7] L. D. Tzuang, K. Fang, P. Nussenzveig, S. Fan, M. Lipson, *Nature Photonics* **8**, 701 (2014).
- [8] E. Lustig, Y. Sharabi, M. Segev, *Optica* **5**, 1390 (2018).
- [9] A. Dutt, *et al.*, *Science* **367**, 59 (2020).
- [10] C. Leefmans, *et al.*, *Nature Physics* **18**, 442 (2022).
- [11] K. Wang, A. Dutt, C. C. Wojcik, S. Fan, *Nature* **598**, 59 (2021).
- [12] Z. Hayran, F. Monticone, *arXiv preprint arXiv:2205.07142* (2022).
- [13] X. Yang, E. Wen, D. F. Sievenpiper, *Physical Review Applied* **17**, 044003 (2022).
- [14] J. S. Martínez-Romero, O. Becerra-Fuentes, P. Halevi, *Physical Review A* **93**, 063813 (2016).
- [15] M. Lyubarov, *et al.*, *Science* p. eabo3324 (2022).
- [16] J. D. Joannopoulos, R. D. Meade, J. N. Winn, *Princeton Univ. Press, Princeton, NJ* (1995).
- [17] D. Sievenpiper, L. Zhang, R. F. Broas, N. G. Alexopolous, E. Yablonovitch, *IEEE Transactions on Microwave Theory and Techniques* **47**, 2059 (1999).
- [18] Y. Sharabi, E. Lustig, M. Segev, *Physical Review Letters* **126**, 163902 (2021).
- [19] R. Carminati, H. Chen, R. Pierrat, B. Shapiro, *Physical Review Letters* **127**, 094101 (2021).
- [20] A. Dikopoltsev, *et al.*, *Proceedings of the National Academy of Sciences* **119**, e2119705119 (2022).
- [21] J. Reyes-Ayona, P. Halevi, *Applied Physics Letters* **107**, 074101 (2015).
- [22] B. Apffel, S. Wildeman, A. Eddi, E. Fort, *Physical Review Letters* **128**, 094503 (2022).
- [23] N. Kinsey, *et al.*, *Optica* **2**, 616 (2015).
- [24] S. Vezzoli, *et al.*, *Physical Review Letters* **120**, 043902 (2018).
- [25] Y. Zhou, *et al.*, *Nature Communications* **11**, 1 (2020).
- [26] See Supplementary Materials.
- [27] I. S. Gonorovsky, *Radio Circuits and Signals* (Imported Pubn, 1982).
- [28] C. Caloz, Z.-L. Deck-Léger, *IEEE Transactions on Antennas and Propagation* **68**, 1569 (2019).
- [29] Y. Sharabi, A. Dikopoltsev, E. Lustig, Y. Lumer, M. Segev, *Optica* **9**, 585 (2022).
- [30] A. Shojaeifard, *et al.*, *Proceedings of the IEEE* (2022).

ACKNOWLEDGMENTS

This work has been supported by the Academy of Finland, project 330260. X. W. and C. R. acknowledge support from the Helmholtz program “Materials Systems Engineering” (MSE). S. F. also acknowledges the support of MURI grants from the U. S. Air Force Office of Scientific Research (Grant No. FA9550-18-1-0379 and FA9550-21-1-0244). The authors would like to thank Dr. Nam Van Ha and Dr. Linping Feng for helpful discussions on the experiment, and Mr. Quangang Chen and Ms. Yining Liu for their kind support in the experiment.